

Local Epitaxial Templating Effects in Ferroelectric and Antiferroelectric ZrO₂

Kisung Chae,^{§§} Sarah F. Lombardo,^{§§} Nujhat Tasneem, Mengkun Tian, Harish Kumarasubramanian, Jae Hur, Winston Chern, Shimeng Yu, Claudia Richter, Patrick D. Lomenzo, Michael Hoffmann, Uwe Schroeder, Dina Triyoso, Steven Consiglio, Kanda Tapily, Robert Clark, Gert Leusink, Nazanin Bassiri-Gharb, Prab Bandaru, Jayakanth Ravichandran, Andrew Kummel, Kyeongjae Cho, Josh Kacher, and Asif Islam Khan*



Cite This: <https://doi.org/10.1021/acsami.2c03151>



Read Online

ACCESS |



Metrics & More



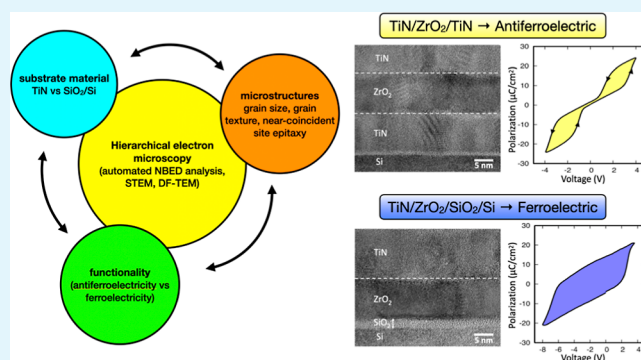
Article Recommendations



Supporting Information

ABSTRACT: Nanoscale polycrystalline thin-film heterostructures are central to microelectronics, for example, metals used as interconnects and high-K oxides used in dynamic random-access memories (DRAMs). The polycrystalline microstructure and overall functional response therein are often dominated by the underlying substrate or layer, which, however, is poorly understood due to the difficulty of characterizing microstructural correlations at a statistically meaningful scale. Here, an automated, high-throughput method, based on the nanobeam electron diffraction technique, is introduced to investigate orientational relations and correlations between crystallinity of materials in polycrystalline heterostructures over a length scale of microns, containing several hundred individual grains. This technique is employed to perform an atomic-scale investigation of the prevalent near-coincident site epitaxy in nanocrystalline ZrO₂ heterostructures, the workhorse system in DRAM technology. The power of this analysis is demonstrated by answering a puzzling question: why does polycrystalline ZrO₂ transform dramatically from being antiferroelectric on polycrystalline TiN/Si to ferroelectric on amorphous SiO₂/Si?

KEYWORDS: nanobeam electron diffraction, high-throughput material characterization, nanocrystalline interface, scanning transmission electron microscopy, hafnium–zirconium oxides



INTRODUCTION

ZrO₂ is an incipient ferroelectric (FE) material, wherein a polar, FE orthorhombic *Pca*2₁ phase is in close energetic competition with an antipolar, antiferroelectric (AFE) tetragonal *P4*₂/*nmc* phase.¹ Consequently, relative phase stability can be altered due to subtle changes in growth conditions, that is, substrate materials. Some of the previous works reported the effects of the substrate on the electrical properties of thin-film hafnia–zirconia alloys.^{2,3} However, these FE oxides are nanocrystalline when deposited as thin films on practical substrates such as nanocrystalline TiN, complicating the fundamental understanding between the microstructure and process optimization. For nanocrystalline growth, the microstructure shows a wide variety of grain sizes and subgrain features, such as domain walls and interphase boundaries, intricately convoluting the relationship between the structure and electronic properties.^{4–7}

In the nanocrystalline, heterogeneous interface between ZrO₂ and TiN, the microstructural evolution of both materials is known to be codependent on grain growth and

crystallization, which mostly occur during postdeposition annealing at elevated temperatures. Due to the large lattice mismatch (~18%) between ZrO₂ and TiN, conventional lattice matching epitaxial growth would be allowed only for specific orientation relationships. ZrO₂⁸ or Hf_xZr_{1-x}O₂ (HZO)⁹(111) grown on TiN(001) would be most favorable due to the lowest level of epitaxial strain. However, other orientations of HZO, such as (100) and (110), are frequently reported on TiN electrodes with mixed TiN orientations of (111) and (001),¹⁰ resulting in a large lattice mismatch. This large lattice mismatch leads to interfacial dislocations for which additional HZO atomic planes match the integral widths of multiple TiN atomic planes. Such a near-coincident site

Received: February 19, 2022

Accepted: July 20, 2022

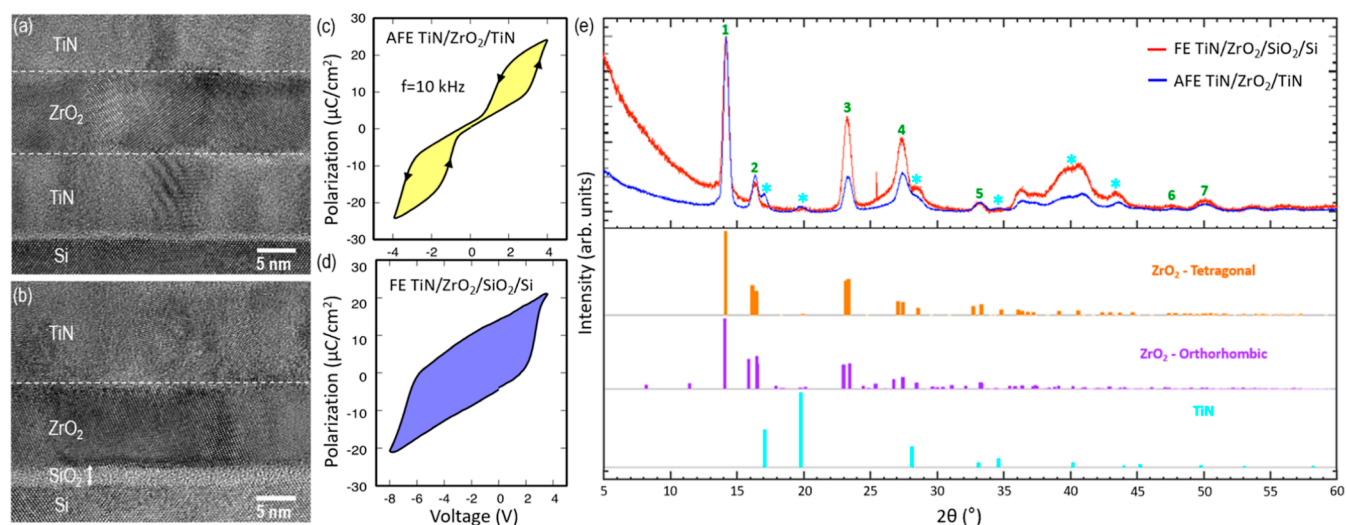


Figure 1. Antiferroelectricity and ferroelectricity in ZrO_2 . HR-TEM images for (a) $\text{TiN}/\text{ZrO}_2/\text{TiN}$ and (b) $\text{TiN}/\text{ZrO}_2/\text{SiO}_2/\text{Si}$ thin-film stacks. Electrical characteristics of polarization–voltage curves show the (c) AFE and (d) FE behaviors for 10 nm thick ZrO_2 on TiN and SiO_2 . (e) A comparison of normalized GIXRD patterns obtained at an incident angle of 0.15° for a 2θ range of $5\text{--}60^\circ$ is shown for 10 nm ZrO_2 MIM (blue) and 10 nm ZrO_2 MIS (red). Diffraction peaks are observed at the expected positions of either tetragonal or orthorhombic, with TiN peaks present for the MIM case. The numbered peaks are those at which the d -spacings of MIM and MIS samples have been compared to those of orthorhombic and tetragonal reference peaks (see the Supporting Information).

epitaxial growth¹¹ has been widely observed in a variety of materials with relatively large lattice mismatch such as semiconductor oxides¹² and oxide–oxide interfaces.^{13–16} Note that lattice epitaxy is a special case of 1/1 near-coincident site epitaxy, where each of the atomic planes in both materials matches with each other at the interface, and the epitaxial relationship between the substrate and deposited film extends for large distances (nearly single crystal).

Atomic-resolution scanning transmission electron microscopy (STEM) is often used to probe atomic-scale epitaxial relationships at the interface of crystalline materials. However, large-scale microstructural analysis over many locations remains a challenge due to the localized nature of STEM data acquisition and the amount of time required to analyze STEM data. It is even more demanding to probe the interface of nanocrystalline materials, which are prevalent in technologically useful material systems such as $\text{TiN}\text{--}\text{HZO}\text{--}\text{TiN}$ capacitors as aligning grains along zone axes for imaging becomes increasingly difficult with a decreasing grain size. In a previous study, nanobeam electron diffraction (NBED) was employed to efficiently investigate the microstructure at the atomic level over a large area for HZO grown on TiN .⁹

NBED provides a series of electron diffraction patterns from evenly spaced grid points, which yields a four-dimensional (4D) stack of data, that is, two-dimensional (2D) scans of 2D patterns. NBED is particularly suitable for high-throughput microstructural characterization because each scan allows for electron diffraction patterns to be collected every few nanometers over micron-sized areas in much less time compared to standard STEM imaging, reducing thermal drift and beam damage effects. However, NBED data can in turn be overwhelming to analyze manually since a single scan may produce thousands of electron diffraction patterns, motivating the development of automated analysis techniques.

Here, a fully automated workflow is demonstrated to determine various epitaxial relations over the polycrystalline interfaces based on NBED data. Starting from individual diffraction patterns, coordinates of each diffraction spot are

obtained to reconstruct the real-space atomic planes at the interface, which are utilized to determine the possible near-coincident site epitaxial growth at each location probed by the electron beam. Using this technique, various types of near-coincident site epitaxies are frequently observed at the $\text{ZrO}_2\text{--}\text{TiN}$ interfaces, revealing consistent structure-directing effects of the nanocrystalline TiN electrode on the ZrO_2 film. Atomic-resolution images obtained by STEM confirm the dominant 3/4 (i.e., matching between three ZrO_2 and four TiN atomic planes) and 2/3 near-coincident site epitaxy at the $\text{ZrO}_2\text{--}\text{TiN}$ interface, consistent with statistics from NBED data.

Applying the developed technique, thin films of $\text{TiN}/\text{ZrO}_2/\text{TiN}$ [metal–insulator–metal (MIM)] and $\text{TiN}/\text{ZrO}_2/\text{SiO}_2/\text{Si}$ [metal–insulator–semiconductor (MIS)] stack structures are compared to investigate the effects of local domain epitaxial growth and their influences on microstructural evolution and functional response. For $\text{TiN}/\text{ZrO}_2/\text{TiN}$, the ZrO_2 microstructure shows active near-coincident site epitaxy at both top and bottom interfaces and has a small grain-to-grain variation in the size with no apparent interfacial layers. In contrast, for $\text{TiN}/\text{ZrO}_2/\text{SiO}_2/\text{Si}$, ZrO_2 grains have predominant lattice matching the top TiN and a large grain size distribution. These changes in the microstructure should alter the relative stability of the polar and the antipolar phases in ZrO_2 , resulting in the observed functional AFE and FE responses on TiN and SiO_2/Si layers, respectively. Density functional theory (DFT) calculations confirm the dominant role of interfacial free energy in phase stability due to the electrode materials, explaining the AFE to FE functional change of the film with the change in the underlying electrode.

RESULTS AND DISCUSSION

Electrical Responses in ZrO_2 . Figure 1a,b shows the cross-sectional high-resolution TEM (HR-TEM) images of the MIM and MIS samples, with distinct interfaces between all layers. The MIM sample exhibits prototypical AFE double-hysteresis loops in its polarization (P) versus voltage (V) characteristics (Figure 1c). Conversely, the MIS sample shows

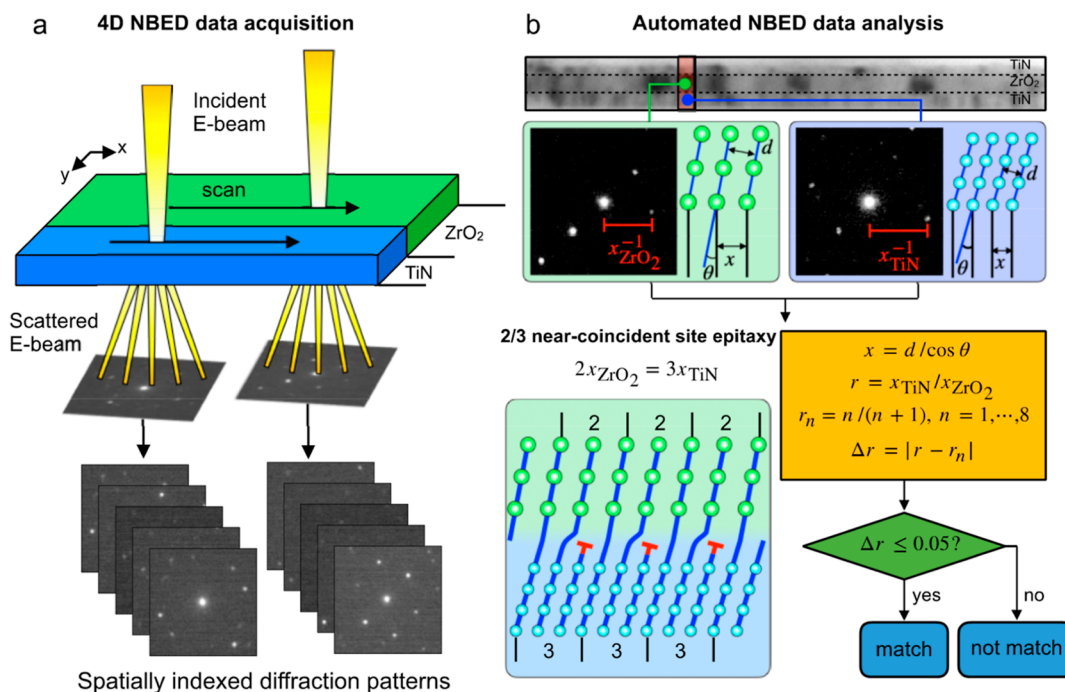


Figure 2. Microstructural analysis based on NBED. (a) Schematic diagram of NBED data acquisition. An electron beam with a nanometer-sized diameter is scanned over a >500 nm length of the cross-sectional samples, producing a series of spatially indexed diffraction patterns. (b) Automated NBED data analysis flowchart. Diffraction patterns across the interface are investigated at each location of the sample to determine the type of near-coincident site epitaxy. Horizontal spacing (x) is computed from the interplanar spacing (d) and the angle of the atomic planes (θ), and the ratio of x in ZrO_2 and TiN (r) is compared with the references (r_n). If the absolute error (Δr) is less than the criterion of 0.05, the corresponding stack is categorized as having a match. Depending on the r value, the type of near-coincident site epitaxy differs, indicating the number of ZrO_2/TiN atomic planes within a domain. An atomic model of the ZrO_2 – TiN interface showing 2/3 near-coincident site epitaxy is shown. Note the additional atomic plane shown in red (\perp) in the TiN region.

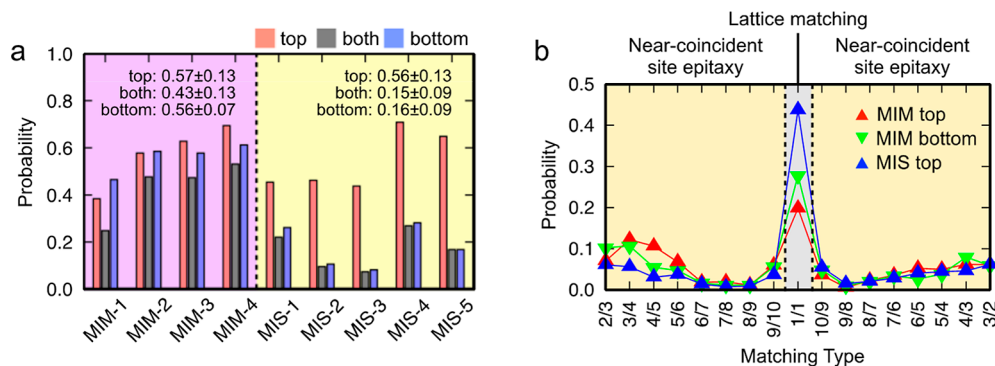


Figure 3. Statistical analysis of the near-coincident site epitaxy from NBED. (a) Probability of near-coincident site epitaxy for each sample. A total of 2064 and 2014 diffractograms are used to analyze the near-coincident site epitaxy in four MIM (ZrO_2 on TiN) and five MIS (ZrO_2 on SiO_2) regions, respectively. All ZrO_2 – TiN interfaces regardless of the structure (MIM or MIS) show an average probability of 0.56, while a much lower probability of 0.16 is observed for the ZrO_2 – SiO_2 interface, which is consistent with the thin amorphous SiO_2 layer shielding the crystalline substrate. Considering some grains have their zone axes misaligned relative to the electron beam direction, a 56% probability of matching at the top interface is consistent with atomic scale matching being prevalent at the ZrO_2 – TiN interfaces. (b) Distribution of the match types at the ZrO_2 – TiN interfaces. Lattice matching, a special case of 1/1 near-coincident site epitaxy, is most prevalent in all cases, while near-coincident site epitaxy of 2/3 and 3/4 is the next most prevalent at the ZrO_2 – TiN interface. The MIS ZrO_2 –amorphous SiO_2 interface is not shown due to the weak signal-to-noise ratio.

a robust, single-loop FE response (Figure 1d). Note that the near-zero remnant polarization is at 0 V for ZrO_2 on TiN (Figure 1c), and a uniform polarization difference in the hysteresis loop is seen throughout the voltages for ZrO_2 on SiO_2 (Figure 1d). The characteristic FE and AFE hysteresis loops shown in Figure 1c,d indicate a substantial difference in the degree of FE versus AFE phases present in the MIS versus MIM samples.

Grazing incidence X-ray diffraction (GIXRD) patterns are shown in Figure 1e for the MIM and MIS samples, from which phase analysis is performed. The fixed incident angle of the GI geometry renders any analysis on the intensities of the reflections meaningless as the orientation of the different diffracted planes would have their normal oriented along different directions. Unless the sample is extremely isotropic, the texture cannot be directly inferred from the intensity ratios.

Similarity scores are obtained between experimental peak positions and those in the reference by considering the respective d -spacings (see the [Supporting Information](#)), where a score of 0 indicates a complete match with that particular phase. Here, it can be seen that the MIS film possesses a score close to the orthorhombic phase, and the MIM film is close to the tetragonal phase. Since the two films have a nonzero similarity score, the possibility of a phase mixture of orthorhombic and tetragonal phases cannot be ignored. However, from the analysis, it can be said with certainty that the MIS film is predominantly orthorhombic and the MIM film is predominantly tetragonal. Additional GIXRD measurements ([Figure S1](#)) show a slight shift of the (111) peak ($2\theta \sim 30^\circ$) to a higher value for ZrO_2 grown on TiN compared to ZrO_2 grown on SiO_2/Si , consistent with the reference peak positions for the AFE tetragonal $P4_2/nmc$ and FE orthorhombic $Pca2_1$ phases.¹⁷ Note that while the (111) peak around $2\theta \sim 30^\circ$ is analyzed for the FE versus AFE peak positions, this is not the exclusive texture of the films as shown below in the STEM analysis.

High-Throughput NBED Analysis Workflow. An automated analysis method for NBED data was developed to investigate near-coincident site epitaxy in heterogeneous interfaces over large sample areas with statistical significance. Electron diffraction patterns were analyzed to determine any epitaxial relations between nanocrystalline ZrO_2 and TiN or Si. For statistical analysis, four TiN/ ZrO_2 /TiN (MIM) and five TiN/ ZrO_2 / SiO_2 /Si (MIS) sample areas with widths over 500 nm were probed. The process is composed of three stages as shown in [Figures 2 and 3](#): (1) NBED data acquisition, (2) automated NBED data analysis, and (3) statistical analysis.

In the data acquisition stage, the nanoscale electron beam probes the focused ion beam (FIB)-processed samples on an evenly spaced grid to generate a series of electron diffraction patterns as shown in [Figure 2a](#). In these experiments, an electron beam with a diameter of approximately 5 nm was scanned on an even grid with a step size of 2 nm in all directions. A total of 2064 ZrO_2 -TiN diffraction pattern pairs and 2014 ZrO_2 - SiO_2 diffraction pattern pairs along the interfaces of ZrO_2 samples grown on TiN and SiO_2 , respectively, were recorded. Note that for NBED, the electron beam direction is fixed with respect to the sample, so additional near-coincident site epitaxy could occur at locations with no crystalline diffraction peaks at the fixed detection angle. Thicknesses of the FIB samples in this study range from 50 to 100 nm, which creates a possible over-counting of the near-coincident site epitaxy due to multiple through-thickness grains being present. It is important to note that a well-known complementary advanced microscopy technique, precession electron diffraction, can offer three-dimensional statistical crystallite analysis in the form of phase and orientation mapping.^{18,19} However, the lamella through thickness compared to the crystallite size may likely result in overlapping of grains, leading to low reliability, and a smaller through thickness with a 10 nm film of interest can result in a poor signal-to-noise ratio. The NBED analysis used here shows statistically significant differences between samples even with the possible presence of over-counting (see the [Supporting Information](#) for detailed discussion).

Electron diffraction patterns can be used to reconstruct the crystal lattice structures of the probed area; microstructural information such as the crystal symmetry, crystallographic orientation, and interplanar spacing can be explicitly obtained

by inspecting the diffraction patterns. Here, an image processing workflow to automatically identify the coordinates of diffraction peaks is developed as follows. By using the electron diffraction data (i.e., intensity distribution in the diffraction pattern) as a 2D potential energy landscape, subsequent Monte Carlo simulations on noninteracting fictitious particles are performed so that clusters of the fictitious particles form around each of the diffraction peaks, as shown in [Figure 2b](#). A density-based spatial clustering of applications with noise (DBSCAN) algorithm,²⁰ as implemented in a Sci-Kit Python library,²¹ is used to separate individual clusters of the fictitious particles to compute the center of mass positions of each diffraction peak. The details and pictorial descriptions of the process can be found in the [Supporting Information](#). After listing all the diffraction peak positions for both ZrO_2 and TiN, located along the same interfacial position within the NBED scan, near-coincident site epitaxy is tested based on the diffraction peak positions. The horizontal distance (x) is varied by the interplanar spacing (d) and rotation angle (θ) as $x = d/\cos \theta$. The ratios of the x values from ZrO_2 and TiN ($r = x_{\text{TiN}}/x_{\text{ZrO}_2}$) are compared at each location along the ZrO_2 -TiN interface and designated as matching if the error (Δr) is less than 5%. Comparing the x values in ZrO_2 and TiN ensures the identification of the matching conditions at the interface regardless of the combination of d and θ resulting in x of each layer, as long as the interface is completely horizontal, which is hypothesized in this present study. Coincidental matching, if any, should be approximately the same for all interfaces. The example in [Figure 2b](#) shows 2/3 near-coincident site epitaxy, where the coherence length is equal to the horizontal distance of two ZrO_2 and three TiN atomic planes. Note the additional atomic plane in the TiN layer marked by a red symbol (\perp).

[Figure 3a](#) shows the probability of epitaxial matching throughout the 2064 and 2014 diffraction pattern pairs at the ZrO_2 interfaces in the MIM and the MIS structures, respectively. [Figure 3a](#) shows a 56% probability of near-coincident site epitaxy for the bottom ZrO_2 -TiN crystalline interface, which is more than 3 \times higher than the probability of near-coincident site epitaxy for the bottom ZrO_2 - SiO_2/Si interface (16%). Note that the SiO_2 layer is a thin amorphous layer formed on top of Si; therefore, near-coincident site epitaxy of ZrO_2 to SiO_2/Si is essentially near-coincident site epitaxy of ZrO_2 to Si through the SiO_2 layer, for which the templating effect by remote Si is expected to be minimal. It is hypothesized that the observed near-coincident site epitaxy of ZrO_2 to the bottom SiO_2/Si is due to the extremely flat surface promoting the aligned growth of ZrO_2 . Interestingly, all the ZrO_2 -TiN interfaces at both the top and bottom TiN in the MIM structure and the top TiN in the MIS structure show a consistent probability of $\sim 56\%$ matching regardless of the location of the TiN layer with respect to the ZrO_2 layer. This indicates a close interaction between TiN grains and the ZrO_2 grains' crystallization over the atomically abrupt interface, which forms mostly in the annealing process at an elevated temperature.

In the MIM structure, it is noted that a significant portion of the matching grains show a simultaneous matching on both interfaces in the same location. Forty-three per cent (43%) of the probed area shows simultaneous matching, which corresponds to over 75% of the grains showing a match to either the top or bottom. Previously, similar correlations between the ZrO_2 and TiN grains have been reported.²² Note

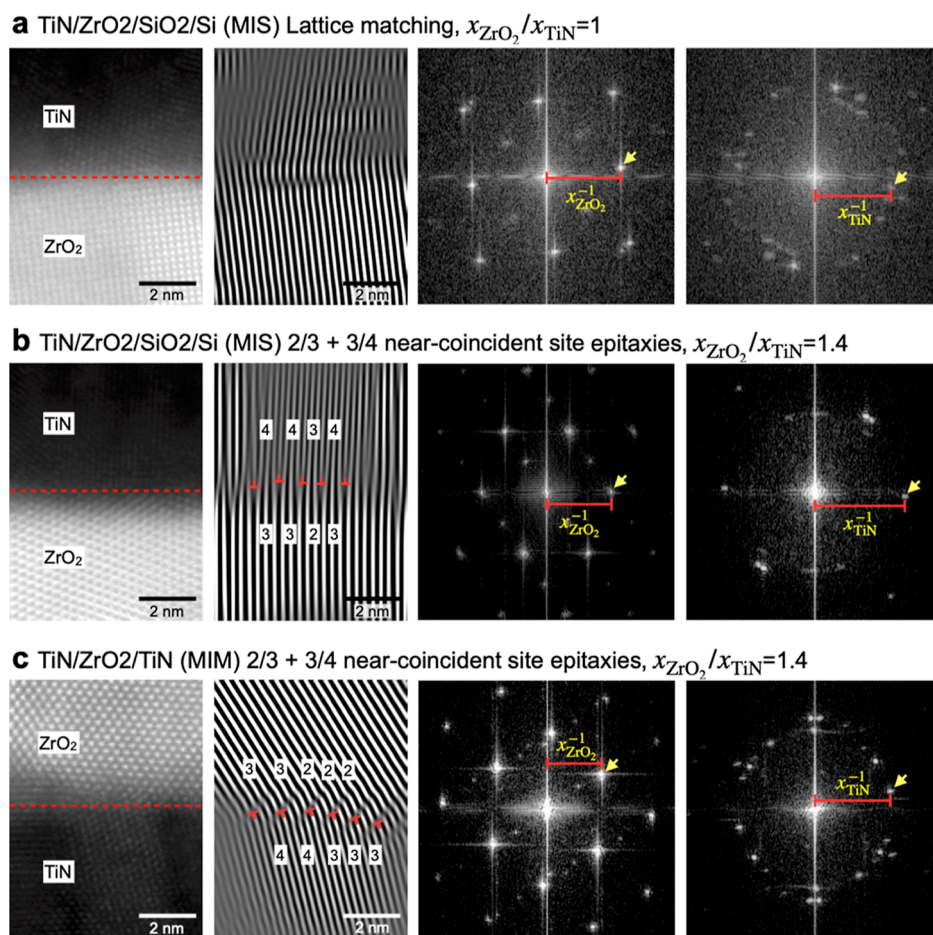


Figure 4. Confirmation of near-coincident site epitaxy at the ZrO₂–TiN interfaces in STEM images. (a) Lattice matching atop the TiN–ZrO₂ interface in MIS, (b) mixture of 2/3 and 3/4 near-coincident site epitaxies at the top TiN–ZrO₂ interface in MIS, and (c) mixture of 2/3 and 3/4 near-coincident site epitaxies at the ZrO₂–bottom TiN interface in MIM. In each set of data, STEM images, Fourier-filtered images, and diffractograms for ZrO₂ and TiN are provided. The horizontal distance (x), inverse of interplanar spacing projected onto the interface, is directly measured from the diffractograms, and the ratio is given in the Fourier-filtered image. The computed ratio agrees well with the near-coincident site epitaxy type observed in the STEM image.

that both the top and bottom TiN layers were deposited by atomic layer deposition (ALD) below 300 °C in the present study (see the [Method](#) section for detailed deposition conditions), while TiN in the other work was deposited by sputtering,²² indicating that the microstructural correlation can be independent of the deposition method if the interfaces are abrupt.

Distributions of the type of near-coincident site epitaxy at the ZrO₂–TiN interfaces are shown in [Figure 3b](#), demonstrating that the conventional lattice matching epitaxy (a special case of 1/1 near-coincident site epitaxy) is most dominant. However, a meaningful portion of near-coincident site epitaxy types is 2/3, 3/4, 4/5, and 5/6, indicating that specific types of non-1/1 near-coincident site epitaxy prevail in the ZrO₂–TiN interface. It is expected that the specific matching types are favored depending on the lattice mismatch and preferred grain orientations to minimize the mismatch. Some of those near-coincident site epitaxy interfaces are directly confirmed in the STEM analysis, discussed below. It is interesting to note that the probability of near-coincident site epitaxy is higher when the ZrO₂ grains are confined by both the top and bottom TiN interfaces (i.e., MIM), while the probability for the lattice matching is highest in the MIS sample. This implies that the near-coincident site epitaxy on one interface can be influenced

by the other interface across the 10 nm ZrO₂ layer, which could promote grain boundary formation and decrease the average grain size (see below).

Direct Observations of Near-Coincident Site Epitaxy in STEM Microstructural Analysis. To confirm the versatile epitaxial relations between ZrO₂ and TiN shown in the NBED analysis, exemplar atomic-resolution STEM analyses are shown in [Figure 4](#). The STEM images are presented in the first column, demonstrating atomically sharp interfaces between ZrO₂ and TiN. The atomic planes showing epitaxy at the interface have finite angles compared to the direction normal to the interface. To highlight those planes, Fourier-filtered images, shown in the second column, are generated using a virtual aperture applied to the Fourier peaks, marked by yellow arrows in the diffractograms. This approach has frequently been used in previous studies to identify the near-coincident site epitaxy.^{11–16} The ratio between x_{ZrO_2} and x_{TiN} (the plane spacing projected onto the interface) is extracted from the images to determine the matching type, as shown in [Figure 2b](#). The ratio obtained at the top interface of the shown MIS structure in [Figure 4a](#) is 1, so lattice matching epitaxy is observed, and the atomic planes of ZrO₂(100) and TiN(111) are lattice-matched.⁹ The same top TiN–ZrO₂ interface in MIS was probed at a different location, showing different

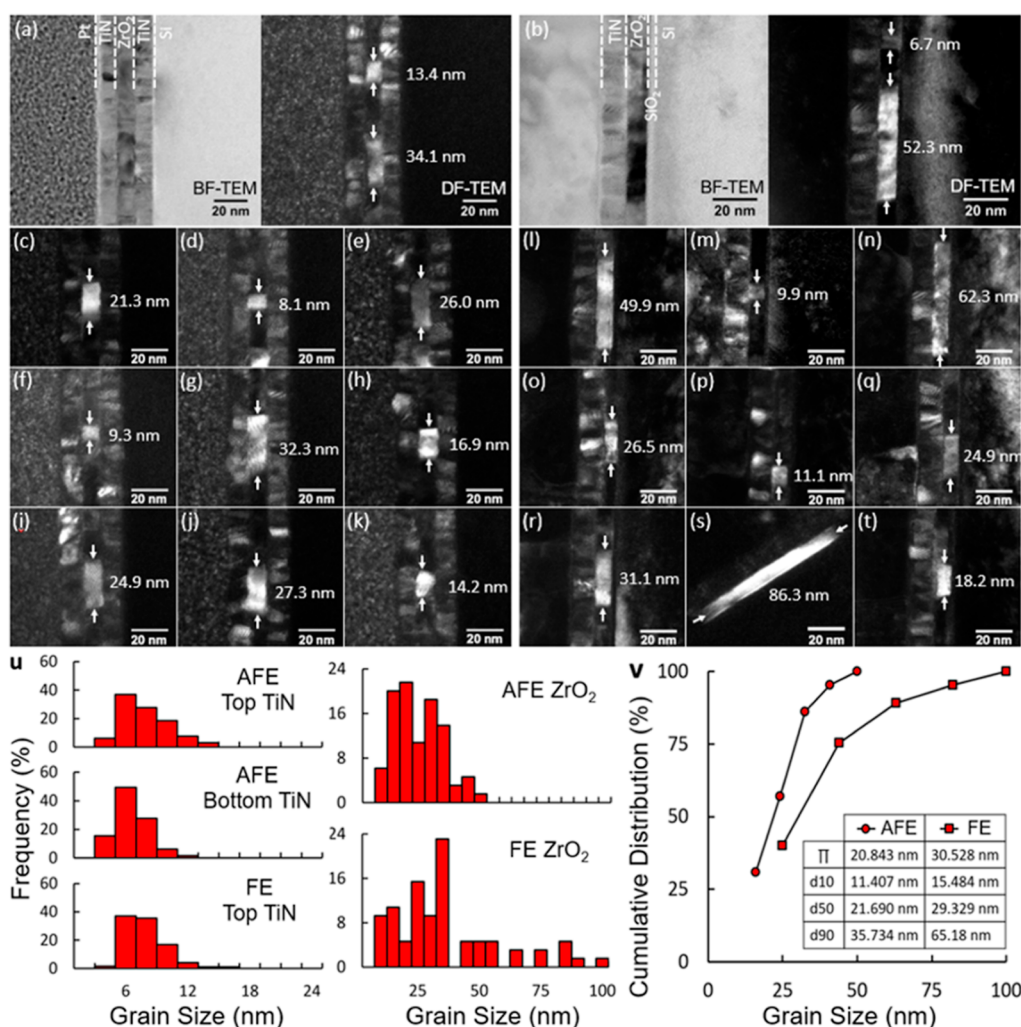


Figure 5. Grain size distributions of ZrO_2 and TiN characterized by TEM. Bright-field (BF) and DF modes of TEM images in (a) MIM and (b) MIS stacks. In the DF mode, the grain size can be measured from the side view due to the high contrast for the grain-to-grain misorientation. DF-TEM images of (c–k) MIM and (l–t) MIS. With a total of 70 measurements per film, grain size distributions for all TiN and ZrO_2 films are obtained as shown in (u). Cumulative distributions of the ZrO_2 grain size (v) show larger grains in MIS (FE) than in MIM (AFE).

epitaxial growth. A $x_{\text{ZrO}_2}/x_{\text{TiN}}$ ratio of 1.4 is observed (Figure 4b), which is best matched to 3/4 (1.33) near-coincident site epitaxy. Compared to ideal ratios, the experimental ratio of 1.4 lies between 3/4 (1.33) and 2/3 (1.5); the difference may be due to stress or strain at the interface. The discrepancy compared to the ideal values is consistent with the coexistence of local domains of 2/3 and 3/4 forming next to each other to compensate the compressive and tensile stresses (Figure 4b). As seen in Figure 4c, atomic planes at the bottom TiN– ZrO_2 interface in MIM also show a mixture of 2/3 and 3/4 near-coincident site epitaxies. In this case, the experimental ratio of 1.4 lies between 2/3 and 3/4, and it can be confirmed that both near-coincident site epitaxy types are observed from the Fourier-filtered image. As mentioned above, microstructures at the ZrO_2 –TiN interface are independent of the relative location within the ZrO_2 thin film.

It is evident that near-coincident site epitaxy is prevalent at the ZrO_2 –TiN interfaces, but elucidating the underlying mechanism is not trivial. First, it is difficult to calculate the free energies of interfaces showing the near-coincident site epitaxy. To develop DFT models, large supercells need to be constructed, and detailed oxygen arrangements at the interface

need to be investigated. Second, at the annealing temperature used in this work (450 °C for 30 s in N_2), the ZrO_2 layer would be kinetically hindered to find the thermodynamic ground states. Rather, the pre-existing (nano)crystalline TiN would direct the crystallographic orientation of ZrO_2 .

Grain Size Statistics by DF-TEM. To probe the grain size distribution, dark-field TEM (DF-TEM) is used as shown in Figure 5, through which individual grains are identified in both the MIM and MIS structures. Here, the grain size is defined by the maximum width of the grain cross-section. Note that DF-TEM is capable of distinguishing one grain from neighboring grains with a large crystallographic misorientation due to the explicitly distinct diffraction patterns. Typically, oxygens are disordered at the high-angle grain boundaries and therefore should show a nonpolar electric response. Based on the measurement of 70 grains for ZrO_2 in each of the sets of MIM and MIS samples, the grain size distributions are shown in Figure 5u. The geometric mean for the grain sizes in ZrO_2 is found to be 20.8 and 30.5 nm for the MIM and MIS samples, respectively. Figure 5v shows the cumulative distribution functions for each case, confirming a wider grain size distribution for the MIS film throughout the 1–100 nm range. This 50% difference in the average grain width

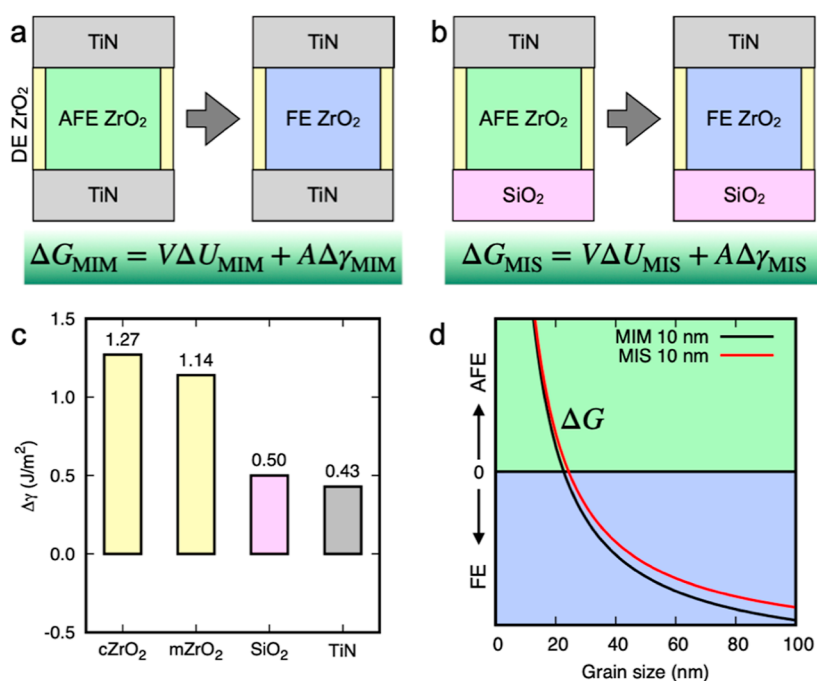


Figure 6. Effects of the grain size and substrate. Schematic diagrams of (a) MIM and (b) MIS where ZrO₂ undergoes a phase transition from AFE to FE, which is exothermic ($\Delta U < 0$) in the bulk state. Cubic ZrO₂ (cZrO₂) or monoclinic ZrO₂ (mZrO₂), shown in yellow, is hypothesized to form at the grain boundaries just as a model DE for simplicity. (c) Interfacial free energy change ($\Delta\gamma$) for cZrO₂, mZrO₂, SiO₂, and TiN calculated by DFT. DE layers (cZrO₂, mZrO₂, and SiO₂) show significant $\Delta\gamma$ due to the electrostatic interactions to FE, while TiN shows very small $\Delta\gamma$ due to its metallic characteristics. (d) Free energy (ΔG) is calculated based on the DFT total energies and interfacial free energies. Overall, AFE is favored for small grains because interfacial effects dominate the overall phase stability, while FE is favored as the grain size increases due to the lower total energy.

corresponds to approximately 2× difference in the grain area and volume.

The smaller average grain size in MIM compared to that in MIS is ascribed to the near-coincident site epitaxy at the interfaces on both sides of the 10 nm ZrO₂ layer, for example, top and bottom TiN interfaces. The MIM near-coincident site epitaxy shown at the ZrO₂–TiN interfaces, as well as the prevalent triple matching (i.e., TiN–ZrO₂–TiN) in Figure 3, is consistent with the confinement of the ZrO₂ grain size. Conversely, for MIS, the amorphous SiO₂ provides flexible interfacial bond formation, spontaneously releasing the bond strain and thereby resulting in larger grain sizes. Various textures of the ZrO₂ film, for example, (001), (011), and (111), are observed from STEM analysis (see the Supporting Information).

Role of the Grain Size in Phase Stability. The most dramatic change in the microstructure of the ZrO₂ film due to different substrates is in the grain size distribution (Figure 6) and the corresponding electrical characteristics due to the phase transformation (Figure 1). To understand the role of the grain size in relative phase stability, a free energy (ΔG) model is developed, similar to previous study,²³ as a function of total energy (ΔU) and differential interfacial free energy ($\Delta\gamma$) as shown in Figure 6:

$$\Delta G(x) = V(x)\Delta U(x) + \sum A(x)\Delta\gamma(x) \quad (1)$$

where x refers to the size of each grain. A and V represent the interfacial area and volume of the grain, respectively. The details of the model are described in the Supporting Information. The AFE to FE phase transition is thermodynamically exothermic in the bulk state, that is, $\Delta U < 0$, but the

change in the interfacial interactions, $\Delta\gamma = (\text{FE}) - \gamma(\text{AFE})$, depends on various factors such as electrical characteristics of the phase and bond strains at the interface. The interfacial interactions have crucial effects on the phase stability as the grain size decreases.²⁴ In the MIS structure, each of the grains has interfaces to either the top or bottom electrodes (TiN or SiO₂) or neighboring grains, so there are three different interfacial free energies: grain boundary, SiO₂, and TiN. Here, it is hypothesized that a dielectric (DE) layer is formed at the grain boundaries as was shown previously.²⁵ This interfacial DE is modeled as the cubic ($Fm\bar{3}m$) ZrO₂ phase to provide computational simplicity since only the electrostatic portion of the interfacial free energy is being considered as in the previous work.²⁶ Figure 6c shows the comparable interfacial free energies between the cubic phase and the monoclinic phase ($P2_1/c$) due to the same DE responses. The sum of $A\Delta\gamma$ terms runs over all the interfaces, that is, top, bottom, and sides. Figure 6c shows that $\Delta\gamma$ is very large for DE ZrO₂ (both cubic and monoclinic phases) and SiO₂ due to the electrostatic interactions with the FE phase. For TiN, even though it has metallic electronic structures, $\Delta\gamma$ is comparable to that of SiO₂ because of the Ti–O bonds at the interface.

Figure 6d shows ΔG as a function of grain size (x). For a small grain size, the AFE phase is favored as the interfacial free energy term dominates. In MIS, $\Delta\gamma$ is greater than that in MIM due to DE SiO₂ on the bottom (Figure 6c). This indicates that a slightly larger grain size is needed to stabilize the FE phase in MIS. The templating effects due to the nanocrystalline TiN electrodes limit the ZrO₂ grain size in MIM where the AFE phase is favored, while larger grains are observed in the MIS structure (Figure 5) favoring the FE phase. Moreover, additional DE interlayer formation such as

TiON at the TiN–ZrO₂ interface would further increase $\Delta\gamma$, making the film prefer the AFE phase due to the unfavorable interfacial free energy between FE and DE. If the film thickness is decreased, the critical grain size is further increased due to an increase in interfacial effects, that is, increased surface-to-volume ratio. However, when the film thickness is decreased down to a few nanometers, the strain becomes a dominating factor, changing the relative energy (ΔU) significantly from that of the bulk.²⁴ In addition to the grain size, the oxygen content also plays a role in the ZrO₂ phase stability, in which oxygen deficiency is observed in the monoclinic and tetragonal phases.^{27,28} Since ZrO₂ films grown on SiO₂ do not experience scavenging effects from the bottom substrate, the ZrO₂ film is expected to contain a higher oxygen content than its MIM counterpart, resulting in the orthorhombic phase being a more likely stable phase in the MIS case.

In summary, the grain size in the 10 nm ZrO₂ thin film interfacing with the nanocrystalline TiN depends critically on the near-coincident site epitaxy, which is shown to exist by using the automated, high-throughput NBED analysis developed in this work. The average grain size is shown to be smaller for the MIM samples with two TiN interfaces when compared with that for the MIS samples with only one TiN interface. The reduced grain size is sufficient to favor the AFE phase over the FE phase, making the ZrO₂ thin film attractive as it can display various electric responses.

CONCLUSIONS

An automated analysis workflow is presented for state-of-the-art NBED, where local crystalline information can be probed by the nanoscale electron beam throughout the sample. The analysis is used to compute the horizontal distances of atomic planes at the interface revealing prevalent near-coincident site epitaxy. Various types of near-coincident site epitaxies are detected automatically over thousands of diffraction patterns and are confirmed by atomic-resolution STEM images. The technique is tested on TiN/ZrO₂/TiN and TiN/ZrO₂/SiO₂/Si interfaces and reveals that not only dominant lattice matching (1/1) but also finite near-coincident site epitaxy (2/3 and 3/4) exist at the ZrO₂/TiN interface, verified by real-space STEM imaging. Over 56% of the samples show atomic scale epitaxial matching, and most of the grains show simultaneous epitaxy on both top and bottom interfaces, indicating confinement in the microstructure. To elucidate the correlations between the microstructure and functionality of ZrO₂ thin films grown on TiN and SiO₂/Si substrates, DF-TEM is used to compute the grain size distribution. Larger grains are observed for ZrO₂ grown on SiO₂/Si showing ferroelectricity, while grain sizes are smaller for AFE ZrO₂ grown on TiN, consistent with lower strain and less near-coincident site epitaxy at the ZrO₂–SiO₂ interface compared to that at the ZrO₂–TiN interface. DFT calculations are used to elucidate the phase stability of the polycrystalline ZrO₂ film on different substrate materials as a function of grain size. It is shown that interfacial free energy plays a crucial role, where the grain size is sensitively influenced by the substrate material. Combined with the high-throughput microstructure analysis technique developed here, statistical analysis of the nanocrystalline interfaces can be done quantitatively, and optimal electrode materials can be investigated for the advancements of emerging microelectronics.

METHODS

Fabrication and Electrical Measurements. 10 nm ZrO₂ thin films were deposited by ALD on a 10 nm TiN layer and on a 1.5 nm chemical SiO₂ layer, both grown on a degenerately doped p+ Si substrate. ALD was performed below 300 °C to ensure the films were nearly amorphous in the as-deposited state. Top TiN layers were subsequently grown on both heterostructures using ALD, followed by sputtering and lithographic patterning of Ti (30 nm)/Au (5 nm) top electrodes for electrical probing; again, TiN ALD was performed below 300 °C to ensure the as-deposited ZrO₂ remained nearly amorphous. Postmetallization annealing was performed at 450 °C for 30 seconds under a N₂ ambient condition for the crystallization of ZrO₂.

Structural Characterization Methods. Cross-sectional samples for imaging were prepared using an FEI Nova Nanolab 200 FIB/scanning electron microscope equipped with a high-energy FIB using Gallium-69 and operated at an accelerating voltage between 5 and 30 kV. The resulting FIB lamellas were approximately 10 μm in length and 50 nm in thickness. BF-TEM, DF-TEM, and HR-TEM images were captured using an FEI Tecnai G2 F30 transmission electron microscope/scanning transmission electron microscope, operated at an accelerating voltage of 300 kV and a beam current of 9 μA . STEM images were collected using a Hitachi HD-2700 aberration-corrected scanning transmission electron microscope/scanning electron microscope, operated at a 200 kV accelerating voltage, 30 mrad convergence angle, and a beam current of 9 μA . Stacks of STEM images were collected to minimize drifting while keeping a reasonable signal-to-noise ratio, each frame taken at integration times between 0.1 and 0.15 s with an image size of 512 \times 512 pixels and each stack containing 30–70 frames. The drift correction was performed using a Hitachi-America (HTA) plugin based on local intensity maxima. GIXRD measurements were performed at the SLAC National Accelerator Laboratory using the Beam Line 2-1 station with a PILATUS 100K detector. An X-ray energy of 17 keV (wavelength of 0.729 Å) is used, with X-rays incident to the ZrO₂ film at an angle of 0.15° for both MIM and MIS samples and also using a Bruker D8 Discover diffractometer with an incidence angle of 0.45° (Cu K α radiation, $\lambda = 0.154$ nm).

NBED scans were collected using an FEI Tecnai G2 F30 transmission electron microscope/scanning transmission electron microscope with an accelerating voltage of 300 kV and a convergence angle of 0.7 mrad. NBED analysis is used to obtain a series of diffractograms from evenly spaced grid points across the TEM cross-sectional samples. Each of the diffractograms is spatially indexed, so the diffraction peak positions from individual grains of ZrO₂ and TiN at the same location can be directly compared. To avoid the overcounting due to the finite size of the electron beam (~ 5 nm in this study), the diffraction patterns are collected away from the ZrO₂–TiN or ZrO₂–SiO₂ interfaces. In each diffractogram, coordinates of the diffraction peaks are found by the Monte Carlo-based optimization method, detailed in the Supporting Information, and are converted to directly compare the width of each domain to determine the matching type.

Simulation Methods. DFT calculations were performed as implemented in the Vienna Ab initio Simulation Package.^{29,30} Exchange-correlation functional of Perdew–Burke–Ernzerhof³¹ was implemented to build the Kohn–Sham Hamiltonian, and the projector augmented wave method was used for the core part of the wave functions.³² The plane waves were expanded up to a kinetic energy cutoff of 450 eV, and the k -points were uniformly sampled within the Brillouin zone at a minimum of 0.032 Å⁻¹ by using the Monkhorst–Pack scheme.³³ The stopping criteria for DFT self-consistent field and conjugate gradient ionic relaxation were 10⁻⁵ meV and 10 meV/Å, respectively.

ASSOCIATED CONTENT

Supporting Information

The Supporting Information is available free of charge at <https://pubs.acs.org/doi/10.1021/acsami.2c03151>.

Additional GIXRD analysis for ZrO₂ in MIM and MIS; multiple grains probed by NBED; automated image processing procedures; additional STEM images for ZrO₂ in MIM and MIS; and thermodynamic phase stability for a model polycrystalline thin film (PDF)

AUTHOR INFORMATION

Corresponding Author

Asif Islam Khan – School of Materials Science and Engineering, Georgia Institute of Technology, Atlanta, Georgia 30332, United States; School of Electrical and Computer Engineering, Georgia Institute of Technology, Atlanta, Georgia 30332, United States; Email: asif.khan@ece.gatech.edu

Authors

Kisung Chae – Department of Chemistry and Biochemistry, University of California, San Diego, California 92093, United States; Department of Materials Science and Engineering, The University of Texas at Dallas, Richardson, Texas 75080, United States; orcid.org/0000-0003-1628-408X

Sarah F. Lombardo – School of Materials Science and Engineering, Georgia Institute of Technology, Atlanta, Georgia 30332, United States

Nujhat Tasneem – School of Electrical and Computer Engineering, Georgia Institute of Technology, Atlanta, Georgia 30332, United States

Mengkun Tian – Institute of Electronics and Nanotechnology, Georgia Institute of Technology, Atlanta, Georgia 30318, United States; orcid.org/0000-0003-2790-7799

Harish Kumarasubramanian – Mork Family Department of Chemical Engineering and Materials Science, University of Southern California, Los Angeles, California 90089, United States; Ming Hsieh Department of Electrical and Computer Engineering, University of Southern California, Los Angeles, California 90089, United States

Jae Hur – School of Electrical and Computer Engineering, Georgia Institute of Technology, Atlanta, Georgia 30332, United States

Winston Chern – Department of Electrical Engineering and Computer Science, Massachusetts Institute of Technology, Cambridge, Massachusetts 02142, United States

Shimeng Yu – School of Electrical and Computer Engineering, Georgia Institute of Technology, Atlanta, Georgia 30332, United States

Claudia Richter – NaMLab gGmbH/TU Dresden, Dresden D-01187, Germany

Patrick D. Lomenzo – NaMLab gGmbH/TU Dresden, Dresden D-01187, Germany; orcid.org/0000-0001-8208-3871

Michael Hoffmann – NaMLab gGmbH/TU Dresden, Dresden D-01187, Germany; orcid.org/0000-0001-6493-3457

Uwe Schroeder – NaMLab gGmbH/TU Dresden, Dresden D-01187, Germany; orcid.org/0000-0002-6824-2386

Dina Triyoso – TEL Technology Center, America, LLC, Albany, New York 12203, United States

Steven Consiglio – TEL Technology Center, America, LLC, Albany, New York 12203, United States

Kanda Tapily – TEL Technology Center, America, LLC, Albany, New York 12203, United States

Robert Clark – TEL Technology Center, America, LLC, Albany, New York 12203, United States

Gert Leusink – TEL Technology Center, America, LLC, Albany, New York 12203, United States

Nazanin Bassiri-Gharb – G.W. Woodruff School of Mechanical Engineering, Georgia Institute of Technology, Atlanta, Georgia 30332, United States; orcid.org/0000-0002-0183-5160

Prab Bandaru – Department of Mechanical & Aerospace Engineering, University of California, San Diego, California 92093, United States

Jayakanth Ravichandran – Mork Family Department of Chemical Engineering and Materials Science, University of Southern California, Los Angeles, California 90089, United States; Ming Hsieh Department of Electrical and Computer Engineering, University of Southern California, Los Angeles, California 90089, United States; orcid.org/0000-0001-5030-9143

Andrew Kummel – Department of Chemistry and Biochemistry, University of California, San Diego, California 92093, United States; orcid.org/0000-0001-8301-9855

Kyeongjae Cho – Department of Materials Science and Engineering, The University of Texas at Dallas, Richardson, Texas 75080, United States; orcid.org/0000-0003-2698-7774

Josh Kacher – School of Materials Science and Engineering, Georgia Institute of Technology, Atlanta, Georgia 30332, United States

Complete contact information is available at:

<https://pubs.acs.org/10.1021/acsami.2c03151>

Author Contributions

§§K.C. and S.F.L. contributed equally to this work.

Notes

The authors declare no competing financial interest.

ACKNOWLEDGMENTS

This work was supported in part by the Applications and Systems-Driven Center for Energy-Efficient Integrated Nano Technologies (ASCENT), one of six centers in the Joint University Microelectronics Program (JUMP), an SRC program sponsored by the Defense Advanced Research Program Agency (DARPA), and in part by the SRC Global Research Collaboration (GRC) program. This work was performed in part at the Georgia Tech Institute for Electronics and Nanotechnology, a member of the National Nanotechnology Coordinated Infrastructure (NNCI), which is supported by the National Science Foundation (ECCS-1542174). This work was in part financially supported out of the State budget approved by the delegates of the Saxon State Parliament. This work was supported in part at both Georgia Tech and USC by a DARPA Young Faculty award no. W911NF2110343 and an IARPA contract no. 2022-21100600004. The grazing incidence diffraction experiments were carried out at the SSRL (beamline 2-1), SLAC National Accelerator Laboratory, supported by the U.S. Department of Energy, Office of Science, Office of Basic Energy Sciences under contract no. DE-AC02-76SF00515.

REFERENCES

- (1) Reyes-Lillo, S. E.; Garrity, K. F.; Rabe, K. M. Antiferroelectricity in Thin-Film ZrO₂ from First Principles. *Phys. Rev. B: Condens. Matter Mater. Phys.* **2014**, *90*, 140103.

- (2) Kim, S. H.; Yu, G. T.; Park, G. H.; Lee, D. H.; Park, J. Y.; Yang, K.; Lee, E. B.; Lee, J. I.; Park, M. H. Interfacial Engineering of a Mo/ $\text{Hf}_{0.3}\text{Zr}_{0.7}\text{O}_2$ /Si Capacitor Using the Direct Scavenging Effect of a Thin Ti Layer. *Chem. Commun.* **2021**, *57*, 12452–12455.
- (3) Yi, S.-H.; Lin, B.-T.; Hsu, T.-Y.; Shieh, J.; Chen, M.-J. Modulation of Ferroelectricity and Antiferroelectricity of Nanoscale ZrO₂ Thin Films Using Ultrathin Interfacial Layers. *J. Eur. Ceram. Soc.* **2019**, *39*, 4038–4045.
- (4) Grimley, E. D.; Schenk, T.; Mikolajick, T.; Schroeder, U.; LeBeau, J. M. Atomic Structure of Domain and Interphase Boundaries in Ferroelectric HfO₂. *Adv. Mater. Interfaces* **2018**, *5*, 1701258.
- (5) Grimley, E. D.; Schenk, T.; Sang, X.; Pešić, M.; Schroeder, U.; Mikolajick, T.; LeBeau, J. M. Structural Changes Underlying Field-Cycling Phenomena in Ferroelectric HfO₂ Thin Films. *Adv. Electron. Mater.* **2016**, *2*, 1600173.
- (6) Lederer, M.; Reck, A.; Mertens, K.; Olivo, R.; Bagul, P.; Kia, A.; Volkman, B.; Kämpfe, T.; Seidel, K.; Eng, L. M. Impact of the SiO₂ Interface Layer on the Crystallographic Texture of Ferroelectric Hafnium Oxide. *Appl. Phys. Lett.* **2021**, *118*, 012901.
- (7) Lederer, M.; Kämpfe, T.; Olivo, R.; Lehninger, D.; Mart, C.; Kirbach, S.; Ali, T.; Polakowski, P.; Roy, L.; Seidel, K. Local Crystallographic Phase Detection and Texture Mapping in Ferroelectric Zr Doped HfO₂ Films by Transmission-EBSD. *Appl. Phys. Lett.* **2019**, *115*, 222902.
- (8) Fan, Z.; Deng, J.; Wang, J.; Liu, Z.; Yang, P.; Xiao, J.; Yan, X.; Dong, Z.; Wang, J.; Chen, J. Ferroelectricity Emerging in Strained (111)-Textured ZrO₂ Thin Films. *Appl. Phys. Lett.* **2016**, *108*, 012906.
- (9) Lombardo, S. F.; Tian, M.; Chae, K.; Hur, J.; Tasneem, N.; Yu, S.; Cho, K.; Kummel, A. C.; Kacher, J.; Khan, A. I. Local Epitaxial-like Templating Effects and Grain Size Distribution in Atomic Layer Deposited Hf_{0.5}Zr_{0.5}O₂ Thin Film Ferroelectric Capacitors. *Appl. Phys. Lett.* **2021**, *119*, 092901.
- (10) Hyuk Park, M.; Joon Kim, H.; Jin Kim, Y.; Moon, T.; Seong Hwang, C. The Effects of Crystallographic Orientation and Strain of Thin Hf_{0.5}Zr_{0.5}O₂ Film on Its Ferroelectricity. *Appl. Phys. Lett.* **2014**, *104*, 072901.
- (11) Narayan, J.; Larson, B. C. Domain Epitaxy: A Unified Paradigm for Thin Film Growth. *J. Appl. Phys.* **2003**, *93*, 278–285.
- (12) Yu, H. K.; Lee, J.-L. Growth Mechanism of MgO Film on Si (100): Domain Matching Epitaxy, Strain Relaxation, Preferred Orientation Formation. *Cryst. Growth Des.* **2010**, *10*, 5200–5204.
- (13) Liu, W.-R.; Li, Y.-H.; Hsieh, W. F.; Hsu, C.-H.; Lee, W. C.; Lee, Y. J.; Hong, M.; Kwo, J. Domain Matching Epitaxial Growth of High-Quality ZnO Film Using a Y₂O₃ Buffer Layer on Si (111). *Cryst. Growth Des.* **2009**, *9*, 239–242.
- (14) Zhang, K. H. L.; Lazarov, V. K.; Galindo, P. L.; Oropeza, F. E.; Payne, D. J.; Lai, H. H.-C.; Egdell, R. G. Domain Matching Epitaxial Growth of In₂O₃ Thin Films on α -Al₂O₃ (0001). *Cryst. Growth Des.* **2012**, *12*, 1000–1007.
- (15) Zapf, M.; Stübinger, M.; Jin, L.; Kamp, M.; Pfaff, F.; Lubk, A.; Büchner, B.; Sing, M.; Claessen, R. Domain Matching Epitaxy of BaBiO₃ on SrTiO₃ with Structurally Modified Interface. *Appl. Phys. Lett.* **2018**, *112*, 141601.
- (16) Estandía, S.; Dix, N.; Chisholm, M. F.; Fina, I.; Sánchez, F. Domain-Matching Epitaxy of Ferroelectric Hf_{0.5}Zr_{0.5}O₂ (111) on La_{2/3}Sr_{1/3}MnO₃ (001). *Crystal Growth & Design* **2020**, *20*, 3801–3806.
- (17) Wang, C.-Y.; Wang, C.-I.; Yi, S.-H.; Chang, T.-J.; Chou, C.-Y.; Yin, Y.-T.; Shiojiri, M.; Chen, M.-J. Paraelectric/Antiferroelectric/Ferroelectric Phase Transformation in As-Deposited ZrO₂ Thin Films by the TiN Capping Engineering. *Mater. Des.* **2020**, *195*, 109020.
- (18) Midgley, P. A.; Eggeman, A. S. Precession Electron Diffraction—a Topical Review. *IUCr* **2015**, *2*, 126–136.
- (19) Jeong, J.; Cautaerts, N.; Dehm, G.; Liebscher, C. H. Automated Crystal Orientation Mapping by Precession Electron Diffraction-Assisted Four-Dimensional Scanning Transmission Electron Microscopy Using a Scintillator-Based CMOS Detector. *Microsc. Microanal.* **2021**, *27*, 1102–1112.
- (20) Ester, M.; Kriegel, H.-P.; Sander, J.; Xu, X. A Density-Based Algorithm for Discovering Clusters in Large Spatial Databases with Noise *Proceedings of the Second International Conference on Knowledge Discovery and Data Mining; KDD'96*; AAAI Press, 1996; pp 226–231.
- (21) Pedregosa, F.; Varoquaux, G.; Gramfort, A.; Michel, V.; Thirion, B.; Grisel, O.; Blondel, M.; Prettenhofer, P.; Weiss, R.; Dubourg, V.; Vanderplas, J.; Passos, A.; Cournapeau, D.; Brucher, M.; Perrot, M.; Duchesnay, E. Scikit-Learn: Machine Learning in Python. *J. Mach. Learn. Res.* **2011**, *12*, 2825–2830.
- (22) Hoffmann, M.; Schroeder, U.; Schenk, T.; Shimizu, T.; Funakubo, H.; Sakata, O.; Pohl, D.; Drescher, M.; Adelman, C.; Materlik, R.; Kersch, A.; Mikolajick, T. Stabilizing the Ferroelectric Phase in Doped Hafnium Oxide. *J. Appl. Phys.* **2015**, *118*, 072006.
- (23) Materlik, R.; Künneth, C.; Kersch, A. The Origin of Ferroelectricity in Hf_{1-x}Zr_xO₂: A Computational Investigation and a Surface Energy Model. *J. Appl. Phys.* **2015**, *117*, 134109.
- (24) Chae, K.; Hwang, J.; Chagarov, E.; Kummel, A.; Cho, K. Stability of Ferroelectric and Antiferroelectric Hafnium–Zirconium Oxide Thin Films. *J. Appl. Phys.* **2020**, *128*, 054101.
- (25) Ushakov, S. V.; Navrotsky, A.; Yang, Y.; Stemmer, S.; Kukli, K.; Ritala, M.; Leskelä, M. A.; Fejes, P.; Demkov, A.; Wang, C.; Nguyen, B.-Y.; Triyoso, D.; Tobin, P. Crystallization in Hafnia- and Zirconia-Based Systems. *Phys. Status Solidi B* **2004**, *241*, 2268–2278.
- (26) Chae, K.; Kummel, A. C.; Cho, K. Hafnium–Zirconium Oxide Interface Models with a Semiconductor and Metal for Ferroelectric Devices. *Nanoscale Adv.* **2021**, *3*, 4750–4755.
- (27) Yashima, M.; Tsunekawa, S. Structures and the Oxygen Deficiency of Tetragonal and Monoclinic Zirconium Oxide Nanoparticles. *Acta Crystallogr., Sect. B: Struct. Sci.* **2006**, *62*, 161–164.
- (28) Wang, J.; Li, H. P.; Stevens, R. Hafnia and Hafnia-Toughened Ceramics. *J. Mater. Sci.* **1992**, *27*, 5397–5430.
- (29) Kresse, G.; Furthmüller, J. Efficient Iterative Schemes for Ab Initio Total-Energy Calculations Using a Plane-Wave Basis Set. *Phys. Rev. B: Condens. Matter Mater. Phys.* **1996**, *54*, 11169–11186.
- (30) Kresse, G.; Furthmüller, J. Efficiency of Ab-Initio Total Energy Calculations for Metals and Semiconductors Using a Plane-Wave Basis Set. *Comput. Mater. Sci.* **1996**, *6*, 15–50.
- (31) Perdew, J. P.; Burke, K.; Ernzerhof, M. Generalized Gradient Approximation Made Simple. *Phys. Rev. Lett.* **1996**, *77*, 3865–3868.
- (32) Kresse, G.; Joubert, D. From Ultrasoft Pseudopotentials to the Projector Augmented-Wave Method. *Phys. Rev. B: Condens. Matter Mater. Phys.* **1999**, *59*, 1758–1775.
- (33) Monkhorst, H. J.; Pack, J. D. Special Points for Brillouin-Zone Integrations. *Phys. Rev. B: Solid State* **1976**, *13*, 5188–5192.